Examination of Spheroidal Graphite Growth and Austenite Solidification in Ductile Iron

JINGJING QING, VON L. RICHARDS, and DAVID C. VAN AKEN

Microstructures of a ductile iron alloy at different solidification stages were captured in quenching experiments. Etched microstructures showed that spheroidal graphite particles and austenite dendrites nucleated independently to a significant extent. Growth of the austenite dendrite engulfed the spheroidal graphite particles after first contacting the nodule and then by forming an austenite shell around the spheroidal graphite particle. Statistical analysis of the graphite size distribution was used to determine the nodule diameter when the austenite shell was completed. In addition, multiple graphite nucleation events were discerned from the graphite particle distributions. Majority of graphite growth occurred when the graphite was in contact with the austenite. Circumferential growth of curved graphene layers appeared as faceted growth fronts sweeping around the entire surface of a spheroidal graphite particle which was at the early growth stage. Mismatches between competing graphene growth fronts created gaps, which divided the spheroidal graphite particle into radially oriented conical substructures. Graphene layers continued growing in each conical substructure to further extend the size of the spheroidal graphite particle.

I. INTRODUCTION

EXTENSIVE research has shown that the solidification of ductile iron is dramatically different from that of a gray iron. Introducing magnesium/cerium to the metal not only changes the morphology of graphite phase but also the solidification process, increasing the complexity of solidification for iron alloys. Gray iron with flake graphite experiences irregular eutectic growth, during which graphite and austenite exhibit competitive growth at the solid–liquid interface.[1–4] Solidification of ductile iron shows divorced eutectic growth of graphite and austenite, and the engulfing austenite isolates the graphite nodule from liquid.[5]

Regarding the nucleation of graphite nodules, some of the first theories postulated that nodular graphite nucleated on a solid phase like iron carbide or supersaturated austenite.[5] There are also many studies supporting that the nodular graphite originates directly from the liquid phase.[6–10] For example, Hecht and Margerie presented evidence that a small graphite nodule formed directly from the liquid phase.[6] Fredriksson, Stjerndahl, and Tinoco showed that graphite nodules were growing in the liquid phase independently from the austenite dendrite for a nickel-alloyed ductile iron.[7] It has also been suggested that growth of the graphite in liquid should be limited due to non-equilibrium conditions.[5,8]

A number of studies have shown that as the austenite and graphite come into contact, the nodular graphite is encapsulated by the austenite. For example, Scheil and Hutter found that nodular graphite was formed directly in the liquid and was later enveloped by austenite in ductile iron.[9] Lux, Mollard, and Minkoff[8] also claimed that the graphite nodules originated from liquid and austenite encapsulated around the primary spheroidal graphite in cast iron. The solidification process involving austenite engulfing the nodular graphite was called the nodule entrapment/encapsulation model.[11–14] In the work by Lux et al., it was suggested that only graphite nodules larger than a certain size (ten microns) would have a complete austenite shell around it, and it isolates the graphite nodule from the liquid.[8]

Encapsulation/engulfment is usually seen in eutectic systems having either one or both phases growing as faceted crystals.[8] As several studies[1,8,15,16] have stated, iron forms nonfaceted austenite dendrites, while carbon forms faceted graphite crystals. This difference leads to an asymmetric eutectic growth zone for gray iron that is skewed toward the graphitic phase in the *Fe-C* phase diagram. Encapsulation occurs around the primary graphitic nodule in hypereutectic ductile irons. The comparable eutectic growth zone for the model of nodular graphite growth with austenite encapsulation extends into the eutectic zone for gray iron.[8] Lux, Mollard, and Minkoff[8] attributed the austenite encapsulation to the faster growth rate of austenite and competitive growth between the austenite and nodular graphite, *i.e.*, non-coupled growth at the solid–liquid interface. Minkoff and Lux[17] suggested that graphite

JINGJING QING, Assistant Research Professor of Metallurgical Engineering, VON L. RICHARDS, Robert W. Wolf Professor of Metallurgical Engineering, and DAVID C. VAN AKEN, Curators' Professor of Metallurgical Engineering, are with the Department of Materials Science and Engineering, Missouri University of Science and Technology, Rolla, MO 65409. Contact e-mail: jq4g5@mst.edu

growth and austenite growth would follow different growth rate laws: (1) the (0001) planes for graphite followed a parabolic growth law; (2) the (10$\bar{1}$0) planes for graphite held an exponential growth law; and (3) austenite followed a parabolic growth law. Based on their discussions, the austenite growth dominated regardless of undercooling in ductile iron.[17] According to Lux, Mollard, and Minkoff, the nonfaceted austenite dendrite propagated easily without too much constraint on the crystallographic orientations, and it grew out quickly to significant size. However, the faceted graphite grew along preferred crystallographic directions; thus, the growth was relatively slow.[8]

Many theories regarding spheroidal graphite growth have been proposed based on empirical observations and general understanding of the solidification process.[17–23] Two well-known models of spheroidal graphite growth include (i) circumferential growth of curved graphene layers around the surface of a graphite nodule,[23] and (ii) spiral growth of the graphene layers in radially orientated helix–cone substructures.[19,24,25] Multi-stage spheroidal graphite growth models describe that there are multiple growth stages following different growth mechanisms for the ductile irons[18,20] or the nickel alloys.[26,27] Some literature mentioned that the formation of spheroidal graphite is driven by the interfacial energy between the graphite and the matrix.[28–31] According to the literature,[30] elimination of surface-active elements like sulfur[32] increases the interfacial energy between the graphite and liquid metal. As a result, a spherical morphology with higher volume-to-surface ratio is more favorable than a flake morphology with low volume-to-surface ratio. However, there is no agreement on the growth mechanism for spheroidal graphite and the actual mechanism remains uncertain.

Previous work by the authors is presented in Reference 33 and the objective of this study is to investigate the solidification process of a hypereutectic ductile iron, especially during the early solidification stages. This paper will offer further evidence of the austenite engulfment process. To retain the structures at various growth stages, quenching experiments were conducted. Automated statistical analyses were performed on over three thousand graphite particles from each specimen and these were measured using a scanning electron microscope equipped with automated feature analysis software. Statistical analysis was used to evaluate the graphite growth at different stages of solidification and the graphite particle size at the moment of encapsulation. Growth mechanisms of the spheroidal graphite were elucidated by deep etching and surface features of the graphite nodules were characterized using high-resolution scanning electron microscopy.

II. EXPERIMENTAL PROCEDURE

A. Mold Design and Simulation Prediction

In a previous study by the authors,[33] spherical ceramic shell molds (of 38 mm inner diameter) were used to interrupt the solidification of a ductile iron alloy.

This previous study showed that the quenching response of the spherical mold was not fast enough to capture the early solidification structures. Therefore, a smaller-sized tubular sampler was adopted to sample and quench the iron alloy in this study. The tubular mold was made using a 10-mm inner diameter quartz tube. Two holes, which worked as the metal inlet and the gas vent, were made on the side of the mold as shown in Figure 1. One thermocouple was installed 55 mm from the end (centered on the cross section) of a tubular mold. The molds were attached to handles to improve sampling during the quenching experiment.

Solidification of ductile iron inside the tubular mold was modeled using computational fluid dynamics software prior to the quenching experiment. Heat transfer coefficient (HTC) between liquid metal and mold was chosen as 3500 W/m^{2}K, assuming there was no air gap along the interface and liquid metal was tightly in contact with the mold.[34] Quench times used in the experiment were estimated based on the simulated cooling curve. Geometry used for the computational simulation and simulated cooling curve are shown in Figure 2.

B. Quenching Experiments

The iron alloy was melted in a 200-lb induction furnace under argon protection. The charge materials included high-purity induction iron (0.002 pct C, 0.006 pct S), pig iron (4.2 pct C, 0.17 pct Si, and 0.006 pct S), Fe75Si (75 pct Si), and graphite (99.9 pct purity). The liquid metal was tapped into a 200-lb ladle at 1763 K (1490 °C) and treated with magnesium-ferrosilicon (46 pct Si, 4.3 pct Mg) and inoculant (73 pct Si, 4 pct Al, and 1 pct Ca).

Fig. 1—A tubular quartz mold used for quenching experiment.

The final composition of the ductile iron used in this study is given in Table I as determined using a Verichek Foundry-Master UV arc spectrometer. Carbon and sulfur contents were determined using a LECO CS600 combustion analyzer, as given by Table I. This experimental alloy was a hypereutectic alloy because the primary phase for this ductile iron was predicted to be the graphite phase, based on the Factsage calculation using version 6.4 and database Factsage FSstel, as given in Figure 3. This iron alloy is similar in composition with the ductile iron used in Reference 33.
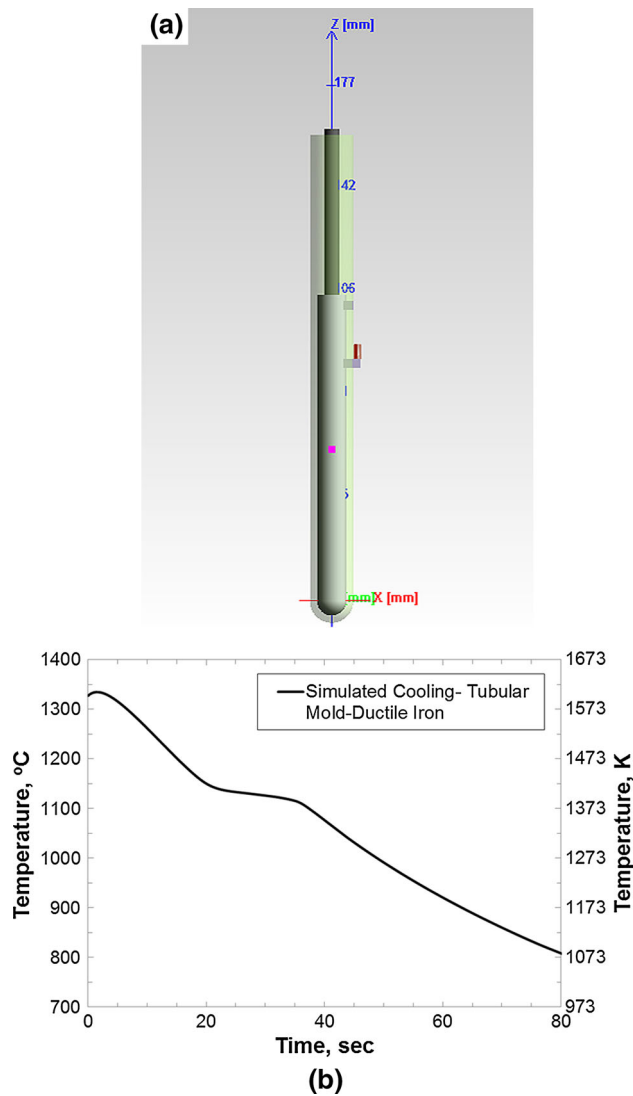
Six tubular molds were preheated by holding their ends (to a depth of ~25 mm) in the liquid metal for 10 seconds, and each simultaneously immersed in the liquid metal at ~1673 K (1400 °C). Upon filling, the six molds were lifted out at the same time from the ladle to minimize experimental variation resulting from inoculant fade or nodulant fade. The lifting out/sampling time was used as the time zero. One mold was quenched into iced brine at 5 seconds after sampling. The other five molds were held inside five individual insulation nests made of kaowool to minimize the external turbulence from the ambient. The additional molds were sequentially quenched at different times: 11, 26, 40, and 60 seconds. Experimental cooling curves for these quenched specimens are shown in Figure 4, which correlate the quenching times with the solidification stages. Eutectic solidification started at 18 seconds (corresponding to the eutectic initiation temperature or TEN[35]), and the solidification ended at 53 seconds (corresponding to the solidus temperature or TS). These critical temperatures were determined from the first derivative of the cooling curve measured for the 60-seconds quenched sample. Based upon these thermal analyses, the 5- and 11-seconds samples were quenched from above the eutectic initiation temperature (TEN), and the 26-seconds sample was quenched at the lowest eutectic temperature (TElow), and the 40-seconds sample was quenched after the metal had reached the highest eutectic temperature (TEhigh), and the 60-seconds sample was quenched after the metal completely solidified at the solidus temperature (TS). The last sample was left to solidify in the insulation nest without quenching, as a comparison to the quenched samples.

Fig. 2—Geometry of a tubular mold (*a*). Simulated cooling curve for an instantaneous fill of ductile iron at 1623 K (1350 °C) (*b*) using the quartz tubular mold (*a*).
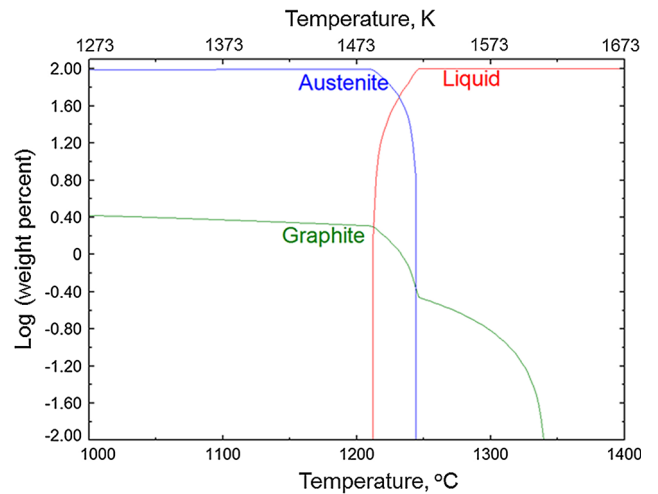

Fig. 3—The primary phase during solidification is graphite for the ductile iron studied, predicted by the Factsage Equilibrium calculation using version 6.4 and database Factsage FSstel.

Table I. Chemical Composition (wt pct) of Ductile Iron Alloy Studied

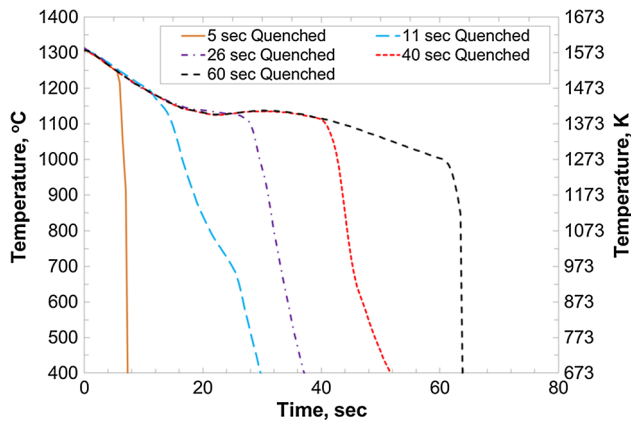| Leco C	Leco S	Si	Mn	Mg	Cu	Al	Cr	Ni
3.67	0.0072	2.32	0.3	0.045	0.6	0.03	0.05	0.04

Fig. 4—Cooling curves of sequentially quenched samples using tubular molds.

C. Metallography

Metallographic specimens were obtained as close to the tip of the thermocouple as possible (usually within 2-mm). Standard metallographic procedures were used with the aim of retaining the graphitic structure. As-polished microstructures were examined by optical microscopy, and using a scanning electron microscopy system equipped with electron dispersive X-ray detector and Automated Feature Analysis software (SEM-EDX-AFA). The AFA software documented a complete EDX spectrum, coordinates, maximum diameter (DMAX), and minimum diameter (DMIN) of each particle. Average diameter (DAVE) of a particle was determined using a rotating chord algorithm which averaged the eight intercept lengths measured along sixteen Chords. The area of a particle was calculated based on the eight intercept lengths. Number of particle ranged from 3093 to 3379 for the sampling and statistical analyses that were performed on the entire population measured. Matrix microstructures were documented using optical microscopy after etching the specimens with 1 pct nital.

D. Deep Etching

Graphite nodules were extracted from the 5-seconds quenched sample (tubular mold) by deep etching and were used to investigate the early graphite growth. Deep etching was performed using a one-gram specimen that was cut from next to the metallographic specimen and deep etched in boiling concentrated hydrochloric acid to remove the matrix. The graphite particles were extracted and rinsed with ethanol. In addition, graphite nodules representative of intermediate and late growth stages were obtained from materials produced in Reference 33. These additional samples were obtained using spherical samplers previously described.[33] These spherical samplers induce a slower cooling rate, and both quenched and unquenched samples from the previous study were deep etched to obtain exemplar graphite nodules from intermediate growth stages and late growth stages of the graphite nodules. A high-resolution scanning electron microscopy (HRSEM) system was adopted to examine the features of the graphite particles.

III. RESULTS AND DISCUSSIONS

As-polished and etched microstructures of the sequentially quenched specimens are given in Figure 5. The as-polished microstructures clearly show that the size of the graphite nodules increased with increasing solidification time, as shown in Figures 5(a) 5-seconds, (c) 11-seconds, (e) 26-seconds, (g) 40-seconds, (i) 60-seconds, and (k) not quenched. Liquid present upon quenching transformed to ledeburite, which is revealed as a composite structure of cementite and pearlite (or martensite) when etched with nital. Austenite formed during solidification was identified by the dendritic morphology and microstructures typical of transformed austenite, i.e., pearlite, bainite, and martensite depending upon the imposed cooling rate during specimen quenching. The evolution of the liquid phase and the austenite phase, can be discerned from the etched images in Figures 5(b) 5-seconds, (d) 11-seconds, (f) 26-seconds, (h) 40-seconds, (j) 60-seconds, and (l) not quenched. Therefore, the presence of a continuous austenite decomposition product (pearlite, bainite, or martensite) next to the graphite was taken as the evidence of an austenite shell. The liquid phase was identified by the carbidic eutectic microstructure commonly referred to as ledeburite in white irons and was only observed in the quenched samples. Based on these observed microstructures, the graphite size and the volume fraction of austenite continuously increased while the liquid fraction decreased during solidification. Figure 5(b) clearly shows that the austenite and graphite phases are independent of each other in the 5-seconds specimen. Austenite shell formation and engulfment of the graphite has started in the 11-second sample as shown in Figure 5(d). Complete engulfment has occurred in the 40-second sample as shown in Figure 5(h) and the distribution of graphite nodules has become clearly bimodal after 40 seconds (see Figure 5(g)).

Smaller-sized graphite nodules (corresponding to the early stages of solidification) and higher fractions of liquid phase were retained using the tubular samplers, as compared with those reported using a spherical mold[33] and early solidification structures were captured in the 5- and 11-seconds quenched samples. The previous study using spherical molds has shown that the austenite phase formed dendrites in the liquid phase, and the austenite was nucleated independently from the graphite nodules during the early solidification stages of the near eutectic hypereutectic ductile iron.[33] The slower cooling rate imposed by the spherical sampler allowed for significant dendritic growth of austenite, which mechanically pushed the graphite until captured by adhesion, which occurred at both dendrite tips and between secondary dendrite arms. Examples of each are shown in Figure 6: graphite nodules trapped between two austenite dendrite arms (as indicated by the dotted circles in Figure 6(a)), and some of the graphite nodules were captured and engulfed by the tip of the austenite dendrite arms (as indicated by the dashed circles in Figures 6(a) and (b)).[33] Completion of austenite shells around a small proportion of the graphite nodules was observed in the 5-seconds quenched specimen, and most
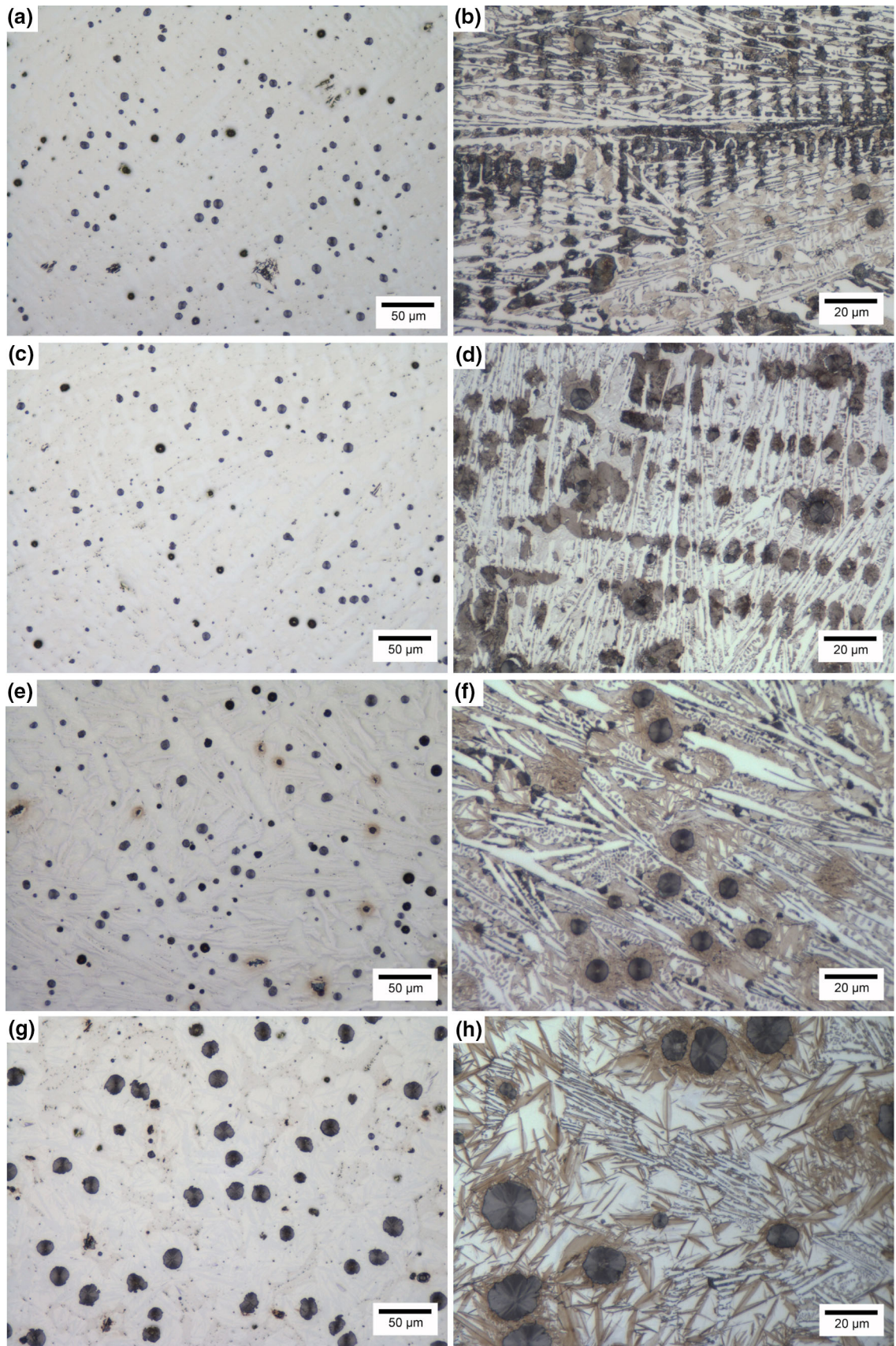
Fig. 5—As-polished microstructures (*a, c, e, g, i, k*) and etched microstructures (*b, d, f, h, j, l*) of specimens quenched at (a-b) 5 s, (c-d) 11 s, (e-f) 26 s, (g-h) 40 s, (i-j) 60 s, and (k-l) without quenching.
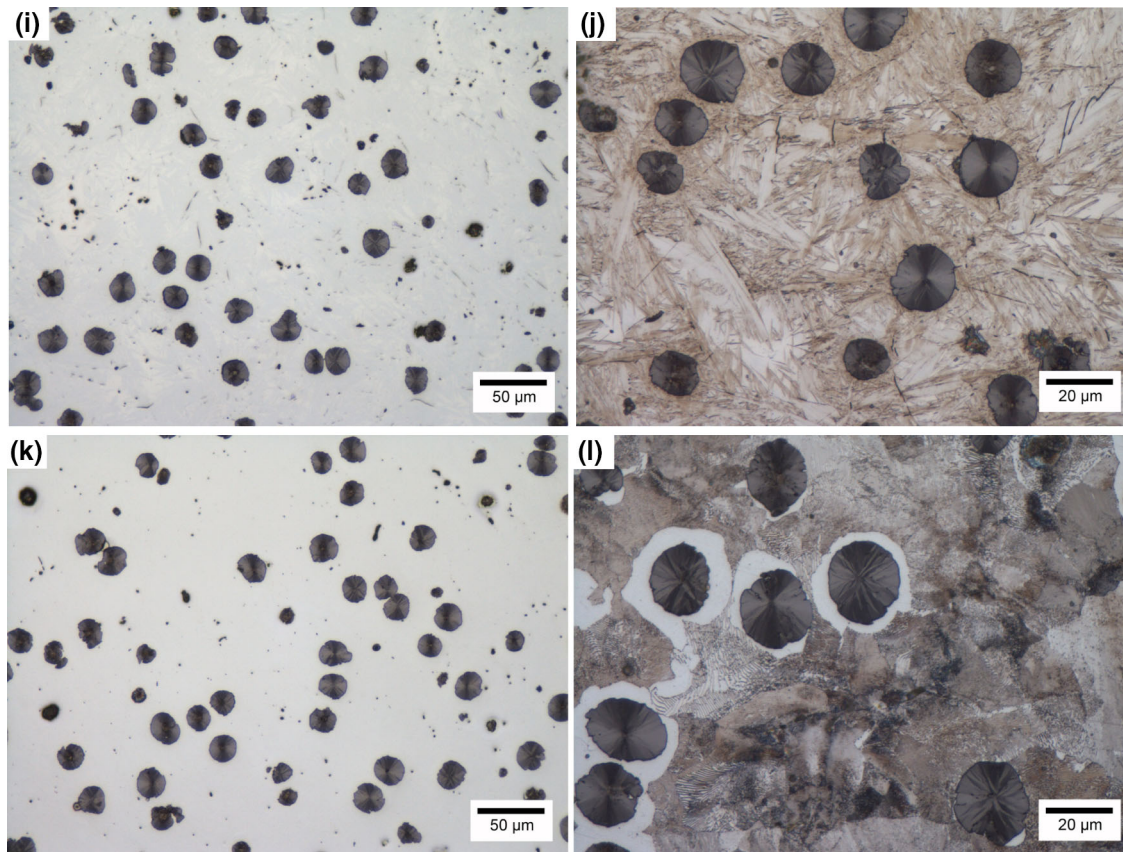
Fig. 5—continued.

of the graphite nodules were isolated from liquid by the austenite shells after 26 seconds. It is generally thought that nodule growth after austenite encapsulation is limited by solid-state carbon diffusion through the austenite.[8] A single austenite dendrite may encapsulate multiple graphite nodules[12,36] and Figure 7 shows an example where multiple graphite nodules are within a single dendrite that is distinguished by interdendritic porosity. In each of the austenite dendrites with multiple graphite nodules, larger graphite particles may coarsen at the expense of small particles, during the eutectic growth. In addition, some graphite particles were agglomerated when contacted by other nodules within interdendritic spaces, which would decrease the nodule count when performed by automated feature analysis. Dendrite impingement occurred near the end of solidification.

A. Graphite Diameter for Austenite Engulfment

Based on the observations in this study, many of the smaller graphite nodules were either fully in contact with the liquid phase or partially engulfed by austenite. Smaller-sized graphite nodules exposed to liquid phase were observed in the 5-, 11-, 26-, and 40-seconds quenched specimens. A series of etched micrographs were examined for the 5-seconds quenched and 25-seconds quenched samples to identify whether a complete austenite shell engulfed the graphite particle. The long axis and short axis of each nodule were measured using the Image-J software. Two hundred and fifty graphite particles (170 particles from 5-seconds quenched specimen and 80 particles from 25-seconds quenched specimen) without complete austenite shells and two hundred and fifty graphite particles (170 particles from 5-seconds quenched specimen and 80 particles from 25-seconds quenched specimen) with complete austenite shells were taken into account for this analysis. The long axis was assigned as the diameter of the graphite nodule, and the ratio of the long axis to the short axis (aspect ratio) was calculated for each particle. The aspect ratio was plotted versus the graphite diameter in Figure 8(a). The size distributions for the graphite particles without complete austenite shells (in black) and for the graphite particles with complete austenite shells (in gray) are given in Figure 8(b). The diameters of the graphite particles without complete austenite shells typically fall into a smaller size range, and their aspect ratios are larger than one, which means their shapes are more prolate. Figure 9 shows examples of the prolate-shaped graphite nodules without complete austenite shells. However, graphite particles with a complete austenite shell tend to be larger in size and they are more spherical with an aspect ratio closer to one. Transition from an incomplete austenite shell to a complete austenite shell occurred at a graphite diameter of six to ten microns, similar to that reported in Reference 33.
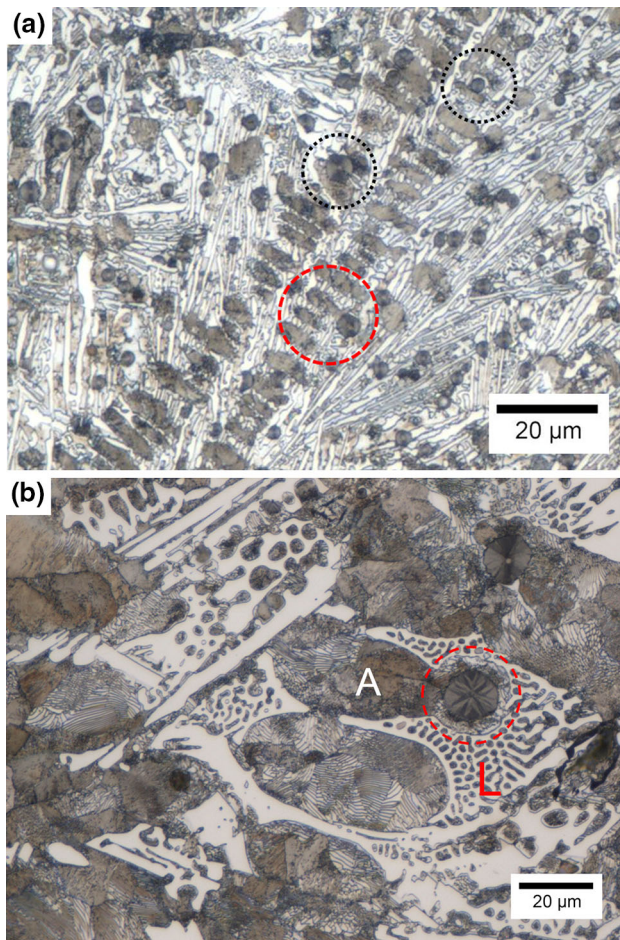
(a)

20 µm

(b)

A

L

20 µm

Fig. 6—Graphite particles trapped between dendrite arms, as indicated by the dotted circles in (*a*). Graphite particles attached on the tip of austenite dendrite arm and engulfed by austenite dendrite arm, as highlighted by the dashed circles in (a) and (*b*), respectively. (b) is reprinted with permission from AFS Transactions.[33] Austenite (transformed to pearlite) is indicated by "A" and the liquid phase (transformed to ledeburite) is labeled as "L".

B. *Anisotropic Growth of Graphite Nodule and Carbon Redistribution*

Graphite nodules partially in contact with liquid phase were normally prolate in shape, with the side facing the austenite protruding further into the austenite,[33] implying anisotropic growth of the graphite particle. This could be related to an asymmetric carbon gradient in the liquid.

Solidification of ductile iron is a non-equilibrium process.[8] If a small undercooling (ΔT) below the equilibrium eutectic temperature (TE) is assumed then the liquid composition would be close to alloy composition (C_0) near the growth front. At the liquid–austenite growth interfaces, the composition of liquid ($C^{L/\gamma}$) would be in equilibrium with the composition of austenite ($C^{\gamma/L}$). At the liquid–graphite interface, the composition of liquid ($C^{L/Gr}$) would be in equilibrium with the graphite composition (C^{Gr}). Composition of austenite ($C^{\gamma/Gr}$) was in equilibrium with graphite composition at the austenite–graphite interface. These
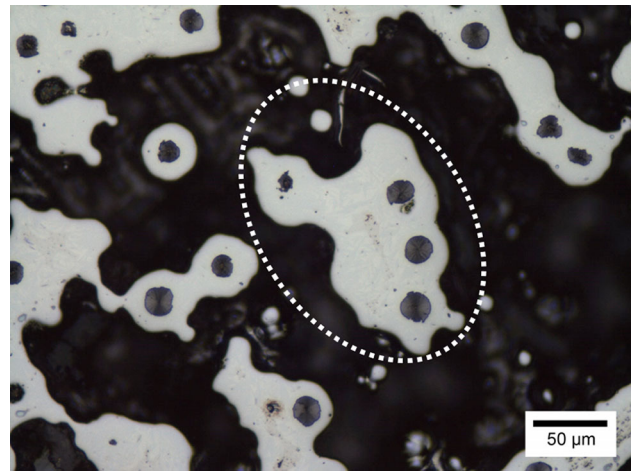

Fig. 7—Multiple graphite nodules were engulfed by a single austenite dendrite, as highlighted by the dotted circle, which is an evidence for multi-nodular eutectic cell model. The dendrite structure was delineated by porosity (dark regions) in the interdendritic regions.

compositions can be estimated from the extrapolated equilibrium liquidus and solidus lines of the stable Fe-C phase diagram, as shown in Figure 10. Factsage was deployed in this study to calculate the carbon concentrations at various interfaces, and the values at 1423 K (1150 °C) are given in Table II. Calculation on graphite nodule growth was performed and the results are shown in the Appendix of this paper.

Illustrations for carbon solute distribution near the growth interface during austenite engulfment were constructed as shown in Figure 11 following a procedure previously demonstrated in References 8 and 37. Solidification of austenite rejects carbon to the austenite–liquid interface, which results in a higher carbon concentration (5.04 wt pct) in the liquid in front of austenite compared to that in austenite (2.35 wt pct), as shown in Figure 11(a). In contrast, growth of the graphite nodule depletes carbon from the surrounding liquid, and a drop on carbon concentration ahead of the graphite nodule (3.11 wt pct) is expected. The carbon solute would redistribute as the austenite growth front approaches the graphite particle. As the austenite–liquid interface approaches the graphite nodule, a carbon concentration gradient would appear in the liquid gap between graphite and austenite. The larger carbon concentration difference of 1.93 wt pct C in front of austenite (in the liquid) will enhance the graphite growth, compared to 0. 56 wt pct C difference on the other side facing liquid. As a result, protrusion of the graphite toward the austenite may occur, as illustrated in Figures 11(b-c). In a similar fashion, austenite growth toward the graphite should also be enhanced. Examples of graphite nodules that protrude toward encroaching austenite dendrite arms are highlighted by circles in Figures 12(a-b). Wetting (adhesion) and engulfment should follow physical contact between graphite and austenite.

A similar argument can be made using the Thompson–Freundlich equation Eq. [1],[38] where the radius of curvature for the nodule is related to a higher
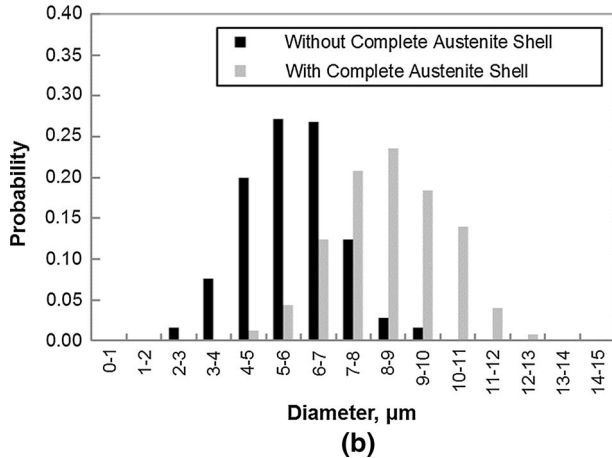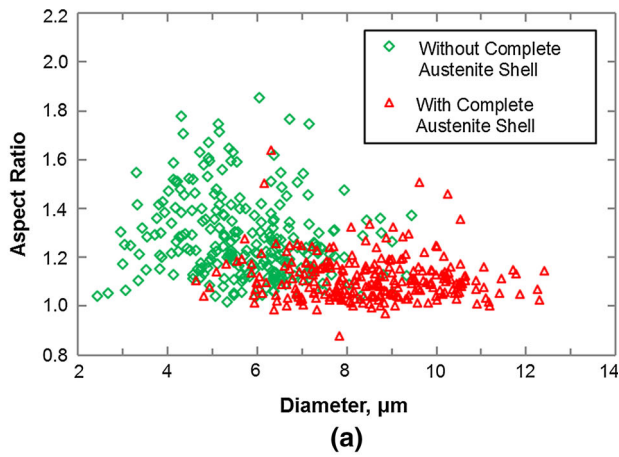
Fig. 8—Aspect ratio (a) and size distribution (b) of graphite particles without a complete austenite shell and with a complete austenite shell. Two hundred and fifty graphite particles were counted for each category.
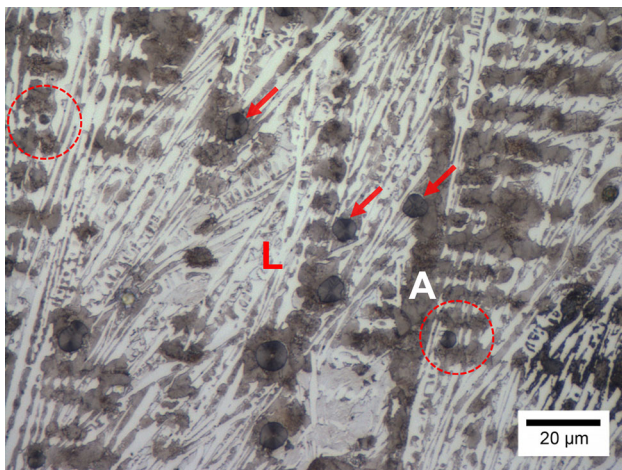

Fig. 9—Graphite particles with incomplete austenite shells, as indicated by the arrows. The graphite nodules highlighted by the dashed circles were trapped between austenite dendrite arms. Austenite (transformed to pearlite) is indicated by "A" and the liquid phase (transformed to ledeburite) is labeled as "L".
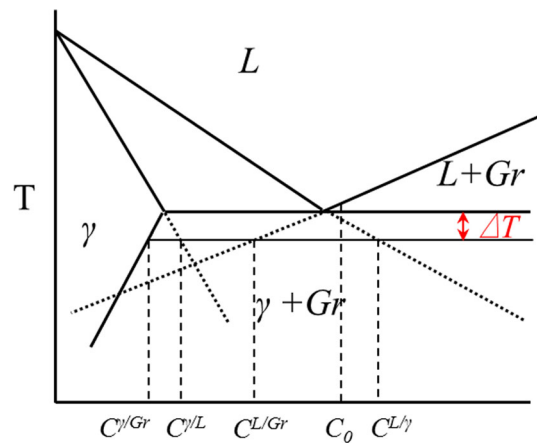

Fig. 10—Schematic diagram of the carbon concentrations at various interfaces predicted by extrapolating the equilibrium Fe-C phase diagram.

carbon concentration in the liquid between the austenite and the graphite than in liquid.

$$r = \frac{2\gamma\delta\Omega}{kT\ln(\frac{c_r}{c})} \qquad [1]$$

The usual definitions are applied to the equation above: r is interfacial radius, γ is surface tension, Ω is atomic volume, T is absolute temperature, c_r is the carbon concentration at the curved interface, c is the equilibrium carbon concentration, and k is the Boltzmann constant. Specifically, this equation argues that as the c_r/c ratio increases, the graphite particle radius should decrease as demonstrated in Figure 11. Thus, a higher carbon activity is expected near regions of high curvature.

Experimental observations in the present study validate the analysis above: graphite nodules with an incomplete austenite shell were prolate, and the side facing the encroaching austenite/liquid interface protrudes further toward the interface. The side facing the austenite in a graphite nodule had a higher curvature (1/r) than the other side facing the liquid phase. A melting point depression may also be expected near the graphite particles due to carbon solute rejected by the solidifying austenite. Upon complete encapsulation of the prolate-shaped nodule by austenite, the nodule would spheroidize to minimize the interfacial surface energy.

One can also consider the effect of graphite particle surface curvature on the local activity of carbon in the austenite near that surface. The high curvature of the graphite tip which formerly faced the advancing austenite now produces a higher local carbon activity in the adjacent austenite if one once again considers the Thompson–Freundlich equation.[38] Thus, the carbon transport in the austenite has a component from the high curvature surface to the lower curvature surface as shown in Figure 11(d), causing the particles to become more dimensionally uniform in all radial directions

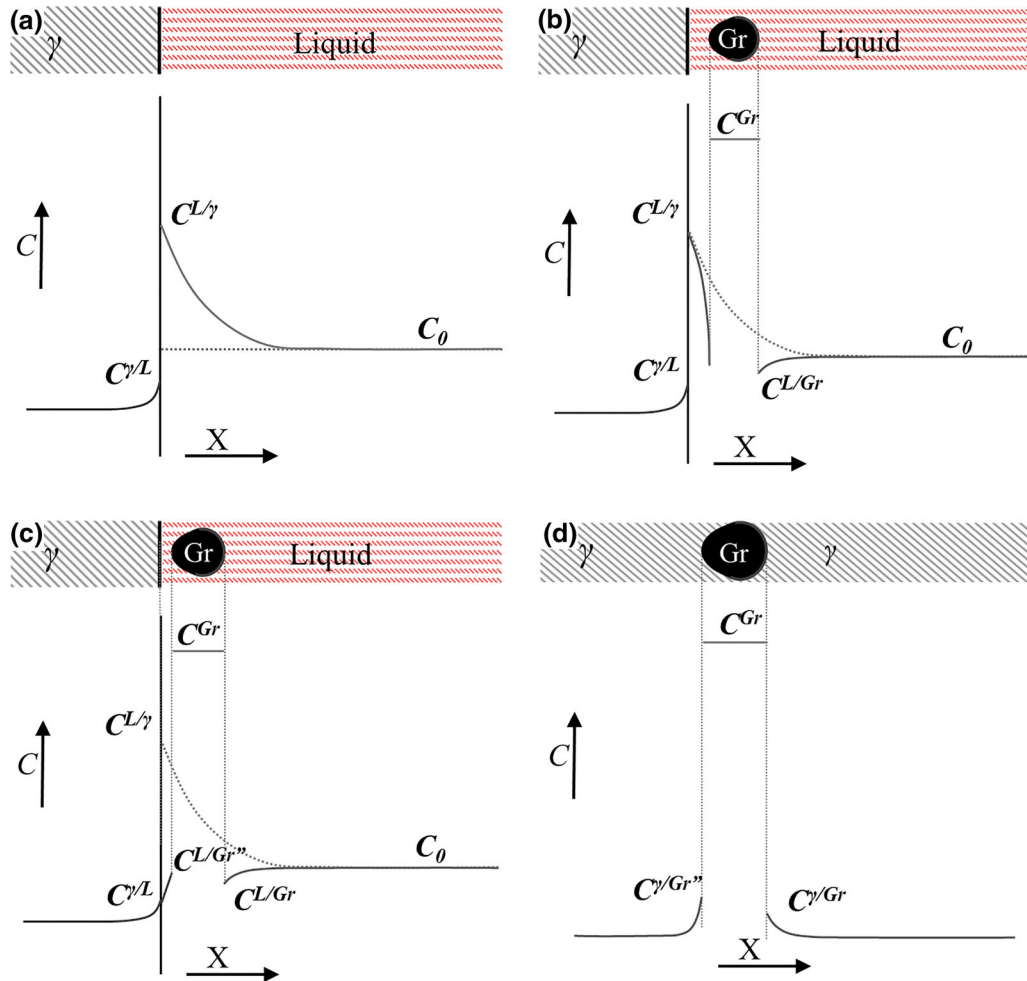| T, K	$C^{L/\gamma}$	$C^{L/Gr}$	$C^{\gamma/L}$	$C^{\gamma/Gr}$	Solid fraction
1423	0.0504	0.0311	0.0235	0.0160	~0.47

Fig. 11—Carbon concentration profile near an austenite–liquid interface (far from graphite particles) (*a*). (*b*) As the austenite growth front approached a graphite particle, growth of the graphite was enhanced on the side facing the austenite compared with the side facing the liquid. Shape of the graphite particle became prolate. (*c*) Carbon solute was redistributed as the graphite nodule protruded toward the austenite. Austenite growth toward graphite was also enhanced. (*d*) After encapsulation of the nodule, carbon transported on the austenite had a component from the higher curvature surface to the lower curvature surface, leading to a more spherical particle, constructed following a procedure previously demonstrated in Refs. 8 and 37.

(more spherical). A step-ledge growth mechanism may also be used to explain the spheroidization of the nodule. The higher curvature side in a prolate-shaped graphite nodule is made of accumulated incomplete growth steps, which now becomes the favored locations for carbon accretion. Thus, carbon accretions would occur on existing growth steps in preference to nucleating new growth steps during the solid-state growth.

This model offers an explanation to the dependence of graphite particle shape on the degree of austenite engulfment. An anisotropic carbon concentration field in the liquid leads to the anisotropic graphite growth. Austenite engulfment occurred as the result of carbon redistribution in front of the interfaces and melting

point depression at the encroaching austenite tip. Furthermore, these prolate-shaped nodules support the hypothesis that the graphite and austenite nucleate independently of each other.

C. Graphite Particle Size Distributions

Graphite nodule size distributions were determined on as-polished specimens using automated feature analysis of back-scattered electron images obtained with the SEM. The composition of each particle was collected using an EDX detector. Features (inclusion, porosity) other than graphite particles were ruled out using a software algorithm and only the graphite particles were

considered for the graphite size distributions. Graphite size statistics were conducted on a sample size of over three thousand particles. The results are plotted in Figure 13. The size distribution of the graphite nodules follows a near normal distribution for the 5- and 11-seconds quenched specimens, where a single-size distribution is observed for each specimen, as shown in Figures 13(a) and (b). In the 5- and 11-seconds quenched specimens both of which were quenched before TEN, the graphite nodule diameters are smaller than 12 μm. Graphite nodules with diameters larger than 12 μm start to appear in the 26-seconds specimen (quenched at the TElow after TEN), but the number counts for the larger-sized graphite nodules (over 12 μm) are very low, as shown in Figure 13(c). Bimodal size distributions, with two distinct distributions, are observed in the 40-seconds quenched specimen (see Figure 13(d)) that was quenched during the eutectic reaction. This suggests that after a first nucleation event occurred prior to the eutectic reaction, a second graphite nucleation event occurred during the eutectic reaction. The primary graphite nucleation event led to only a single graphite distribution peak in the 5- and 11-seconds quenched specimens. The peak corresponding to
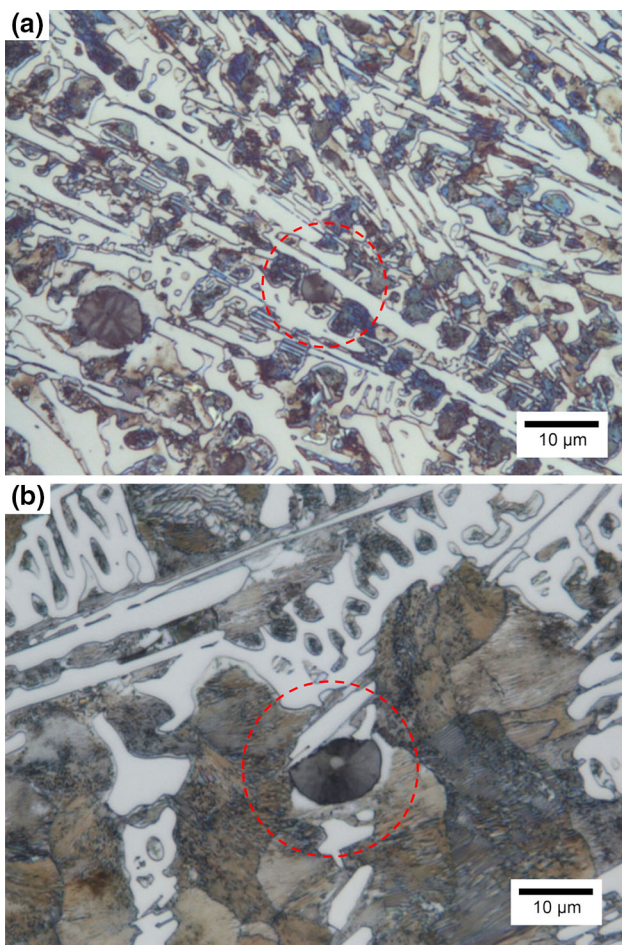

Fig. 12—Examples of graphite nodules protruding toward encroaching austenite, as highlighted by circles in (a) and (b). Both particles are surrounded by liquid.

the primary graphite nucleation gradually shifted to larger size as these primary graphite particles grew. As the eutectic reaction started (corresponding to TEN on the cooling curve), the eutectic graphite nucleation event created a second peak and smaller size distribution. Both the first and the second size distributions moved to larger size range as the graphite particles continued to grow, see Figure 13(e). The sizes of the eutectic graphite particles were catching up with the sizes of the primary graphite particles (compare Figures 13 (d) and (e)). As a result, the second size distribution tended to merge into the first size distribution peak in the unquenched specimen, making it hard to differentiate the two different nucleation events as shown in Figure 13(f). There actually existed a third distribution in Figures 13(e) and (f), which occurred during the later stage of eutectic reaction, see the smaller-sized distribution (approximately between 1 to 9 μm) in Figure 13(f), which suggests that there might be two eutectic nucleation events during the eutectic solidification. Recoalescence during the eutectic reaction may slow the nucleation of graphite such that graphite growth dominates. Upon further undercooling after recoalescence, nucleation resumes creating a third distribution of nodule size.

Statistical analyses over three thousands of graphite nodules shown in this study prove that there are multiple distributions of graphite nucleation during ductile iron solidification. Multiple nucleation events in a ductile iron have been previously reported by the authors.[33,39] It should be noted that the number of size distributions on the graphs may vary depending on alloy composition, cooling rate, inoculation practice, and nucleation practice[39] and that these observations are not unique. Wetterfall et al.[40] mentioned successive graphite nucleation in quenching experiments and Lux et al.[8] discussed the progressive nucleation of graphite in an isothermal process.

Graphite area percent, average graphite diameter, and nodule count were determined for the same ~3000 particles measured for each specimen. Graphite area percent (see Figure 14(a)), average graphite diameter (see Figure 14(b)), and nodule count (Figure 14(c)) did not show significant changes between 5 and 11 seconds when many of the graphite nodules were exposed to liquid: (1) the graphite area fraction was 1.63 pct in the 5-seconds quenched specimen and 1.54 pct for the 11-seconds quenched specimen; (2) the average graphite diameter was 4.68 μm in the 5-seconds quenched specimen and 4.66 μm for the 11-seconds quenched specimen; and (3) the nodule count was 829/mm^2 for the 5-seconds quenched specimen and 810/mm^2 for the 11-seconds quenched specimen. The size distribution also showed little change between 5 seconds (see Figure 13(a)) and 11 seconds (see Figure 13(b)), prior to the eutectic reaction (corresponding to TEN at 18 seconds). This implies that the graphite growth was insignificant before the initiation of eutectic reaction. This might be a result of limited graphite growth in the liquid under a non-equilibrium condition as previously suggested.[5,8] Alternatively, it is possible that the initial graphite nucleation process consumed significant
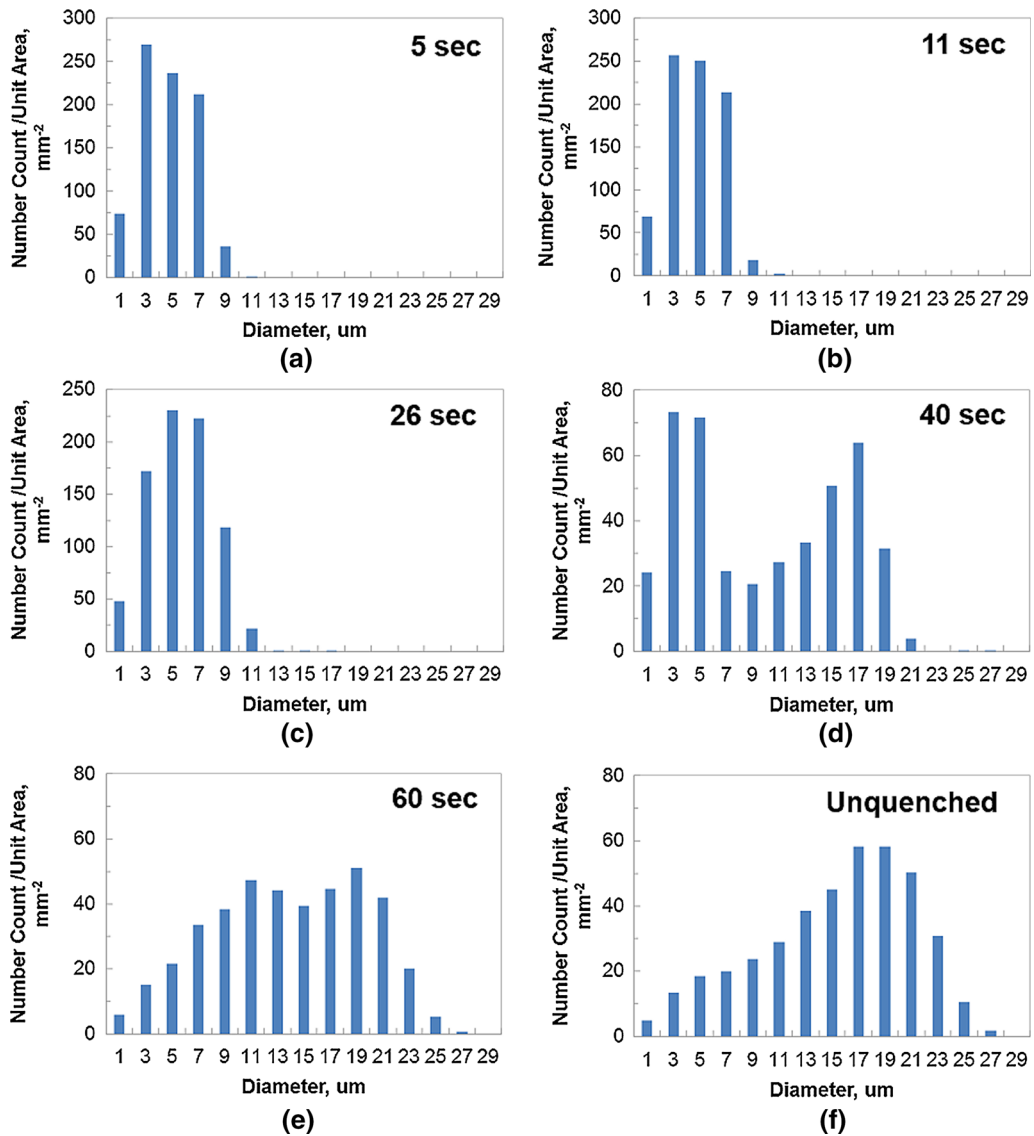
Fig. 13—Graphite nodule size distributions in ductile iron quenched at 5 s (*a*), 11 s (*b*), 26 s (*c*), 40 s (*d*), 60 s (*e*), and without quenching (*f*).

amount of carbon solute, and as a result hindered both growth and further nucleation of the graphite nodules. Moreover, the populations of the graphite nodules in unit volume (nodule count) were slightly decreased between 5 and 11 seconds, which might be a result of coalescence and "ripening" of the graphite nodules if no more graphite nodules were nucleated. It may also be possible that the additional graphite nodules nucleated but the number count of newly nucleated graphite nodules was not able to compensate the loss due to particle coalescence and "ripening." Or perhaps, the primary nucleation density is related to the presence of the inoculating agent, which may also have a size distribution and was exhausted during the first nucleation event. The liquid fractions were estimated on the etched micrographs using the Image-J software, and the liquid fraction continuously decreased during solidification as in Figure 15. It should be noted that the liquid fraction would decrease to zero as the solidification ended at 53 seconds.

Once the eutectic reaction began at 18 seconds, the graphite area fraction and the graphite particle sizes started to increase but the nodule count began to decrease. Based on previous analysis, smaller-sized graphite nodules (diameter smaller than six microns) were normally surrounded by liquid phase, while the graphite nodules engulfed by the austenite dendrites were larger in size. As the eutectic reaction started, a higher fraction of graphite nodules were encapsulated in the austenite phase, and growth of the two eutectic phases, graphite and austenite, followed a divorced eutectic growth mechanism. The graphite area fraction and the graphite diameter is shown to increase after 26 seconds, which indicates significant graphite growth during eutectic reaction in comparison to growth prior to the eutectic reaction, as given in Figures 14(a) and (b). Distinct graphite growth occurred as the graphite was growing inside the austenite phase. In the specimens quenched after the initiation of eutectic reaction (18 seconds) but before the completion of solidification (53
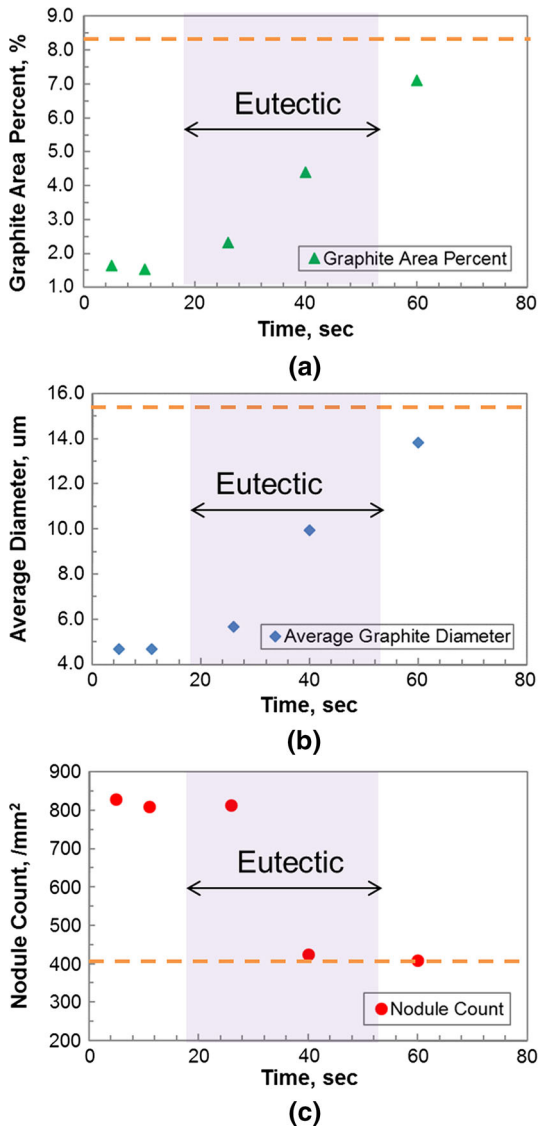
Fig. 14—Area fraction (*a*), average graphite diameter (*b*), and nodule count (*c*) were determined over the area in which 3000 particles were counted. The graphite area percent is 8.3 pct and the average graphite diameter is 15.3 microns, and the nodule count is 402/mm² for the unquenched sample, as indicated by the orange dashed lines.
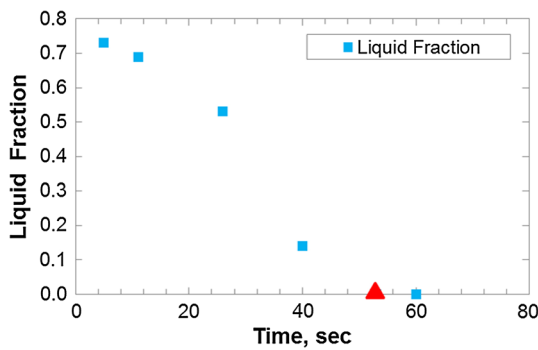

Fig. 15—Liquid fraction decreased during solidification.

seconds), smaller-sized graphite nodules in contact with liquid were observed in the remnant liquid phase, which might be the graphite nodules nucleated in the remnant liquid phase during a second eutectic nucleation event (or a third nucleation event). The nodule count decreased between 26 and 60 seconds, which might be due to agglomeration of graphite nodules, or coarsening of graphite nodules in the same austenite dendrite. Nodule count change between 11 seconds (810/mm²) and 26 seconds (814/mm²) was statistically insignificant. This implied that the decrease of graphite nodule count due to coarsening was compensated by the nucleation of graphite particles in the second nucleation event. However, further drop of the nodule count that resulted from coarsening or agglomeration was not compensated by further nucleation of graphite nodules in the remnant liquid after 26 seconds. The nodule count dramatically decreased between 26 seconds (814/mm²) and 40 seconds (425/mm²), and the liquid fraction also showed a dramatic drop (from 0.53 at 26 seconds to 0.14 at 40 seconds) at the same time. The remnant liquid fraction was low (~0.14) in the 40-seconds quenched specimen, and majority of the graphite nodules were engulfed by the austenite phase, including those later-nucleated graphite nodules corresponding to the second size distribution (smaller sizes), with only few small nodules in contact with liquid. The later-nucleated graphite nodules (smaller than 10 μm in Figure 13(d) and smaller than 16 μm in Figure 13(e)) continued growing. Their sizes were approaching the sizes of the early nucleated graphite from 40 to 60 seconds (larger than 10 μm in Figure 13(d) and larger than 16 μm in Figure 13(e)). The average graphite particle diameter increased from 10.0 to 13.8 μm between 40 and 60 seconds, with a similar growth rate as that between 26 and 40 seconds. However, the nodule count change between 40 seconds (425/mm²) and 60 seconds (409/mm²) became insignificant as the end of solidification was approached. It might be possible that the larger-sized nodules grew at the expense of fine-sized graphite nodules by Ostwald ripening, particularly once the graphite nodules were surrounded by the same, continuous austenite matrix. Once this happens, the carbon activity in the austenite near the graphite particle is affected by the radius of curvature of the particle. Smaller particles produce a higher carbon activity, driving diffusion from the small particles to the large particles.

After the metal completely solidified at 53 seconds, change of the nodule count became small but the graphite nodules kept growing during solid-state reaction, during which the carbon atoms from adjacent austenite added onto the graphite nodule as the solubility of carbon in austenite decreased with temperature and the depleted region adjacent to the nodule transformed to ferrite at the final eutectoid end temperature. The graphite area percent increased from 7.1 pct in the 60-seconds quenched sample to 8.3 pct in the unquenched sample, and the graphite diameter increased from 13.8 μm in the 60-seconds quenched sample to 15.3 μm in the unquenched sample. This
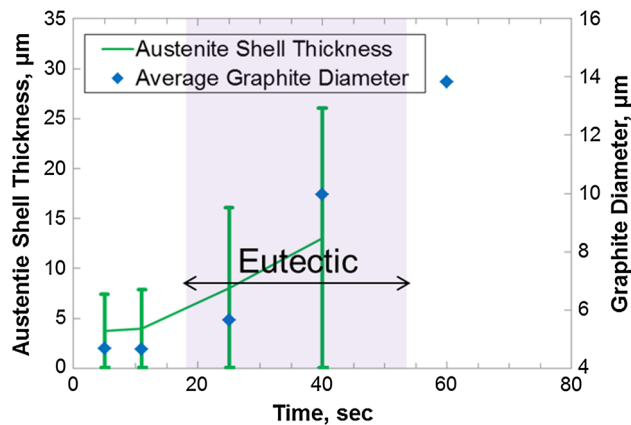
Fig. 16—Austenite shell thickness increased concurrently with graphite diameter during solidification.

implies the growth of graphite nodules during solid-state reaction after solidification. The insignificant change on nodule count (from 409/mm^2 in the 60-seconds quenched sample to 402/mm^2 in the unquenched sample) indicated that there was negligible graphite particle coalescence/coarsening that occurred during the solid-state reaction.

The shape of the austenite shell around graphite was approximated to be quasi-spherical, thus a 2-dimension section of the austenite shell is approximately round. Austenite shell thickness was statistically measured for 100 particles from the quenched sample on the etched micrographs using the ImageJ software, as shown in Figure 16. The minimum austenite shell thicknesses for 5-, 11-, 26-, and 40-seconds specimens equaled zero, because of the existence of the graphite nodules fully in contact with liquid without the surrounding austenite shells. Liquid fraction was zero for the 60-seconds quenched specimen after the solidification completed at 53 seconds, and the austenite shell structure was not recognizable in the 60-seconds quenched specimen. Based on Figure 16, the austenite volume expanded concurrently with the growth of encapsulated graphite inside the austenite.

D. Austenite Engulfment and Interface Instability

Swain and Bates[31] have shown previously that the graphite-liquid interfacial energy is higher in ductile iron (1460 erg/cm^2) than that in gray iron (1270 erg/cm^2). Many studies have shown that droplets of liquid ductile iron did not wet graphite at temperatures below 1473 K to 1773 K (1200 °C to 1500 °C).[30,31,41,42] Contact angles larger than 90 deg measured for liquid iron alloy on a graphite substrate increased with decreasing temperature.[42] Based on Reference 43, austenite engulfment around the graphite nodules requires the graphite–austenite interfacial energy to be lower than the graphite–liquid interfacial energy. Therefore, the graphite–liquid interface in ductile iron is not stable in the presence of austenite and upon contact with austenite, the graphite nodule would become engulfed.

One may argue that the austenite should nucleate directly on a graphite nodule, because of the high graphite–liquid interfacial energy. It is challenging to prove or disprove this, because of the difficulties of finding the heterogeneous nucleation site for large austenite dendrites on polished sections. However, the statistical analysis of the aspect ratio, size distribution, and prolate shape of the graphite relative to the encroaching austenite support a model of independent nucleation of the austenite from graphite. Furthermore, the presence of nitrides, spinels, and sulfides would provide ample heterogeneous nucleation of the austenite.

E. Deep Etching Results and Graphite Growth Mechanism

The 5-seconds quenched specimen from the tubular sampler was deep etched for extracting the graphite particles retained at early growth stages (smaller-sized graphite nodules). Another quenched specimen taken with a spherical sampler and an unquenched specimen sampled with a spherical sampler (which have slower cooling rate than the tubular samplers) were also deep etched for extracting the graphite particles retained at their intermediate growth stages and at their later growth stages.

Examination of the graphite nodules extracted by the deep etching method revealed differences in the surface features of the different sized spheroidal graphite particles which could relate to changes in growth mechanism. For example, growth ledges/steps/fronts made of curved graphene layers wrapping around the surfaces were observed in the smaller-sized graphite particles, as indicated by the arrows in Figures 17(a) and (b), and no substructures were evident in the smaller-sized graphite nodules. The diameters of the graphite particles are six microns and nine microns in Figures 17(a) and (b), respectively. The growth steps observed on the particle surfaces were faceted and they propagated circumferentially around the surfaces of the spheroidal graphite particles. Multiple growth steps were seen on the surface of a smaller-sized graphite nodule, and hole-like defects were observed in the smaller-sized graphite nodule in Figure 17(a) (highlighted with the dashed circle). In a spheroidal graphite particle of 20 μm diameter as shown in Figure 17(c), growth steps and gap-like defects (in the dashed circle) were discernible at the surface. Many gap-like defects were seen in a spheroidal graphite particle of 31 μm diameter, as shown in Figure 17(d). These gaps divide a graphite nodule into conical substructures. Radially oriented conical substructures were distinct in the larger-sized graphite nodule. Faceted growth steps stacked along the radial directions of the nodules were identified either on the surface or in the gaps (see Figure 18) for a larger-sized graphite nodule. Examples are given for a graphite nodule of 74 μm diameter (see Figure 17e) and a graphite nodule of 80 μm diameter (see Figure 17f).

Based on these observations, initially the curved graphene layers grew circumferentially around the entire surface of a spheroidal graphite particle during its early growth stages. It has been seen that the sources from which the growth ledges proceeded were not singular.
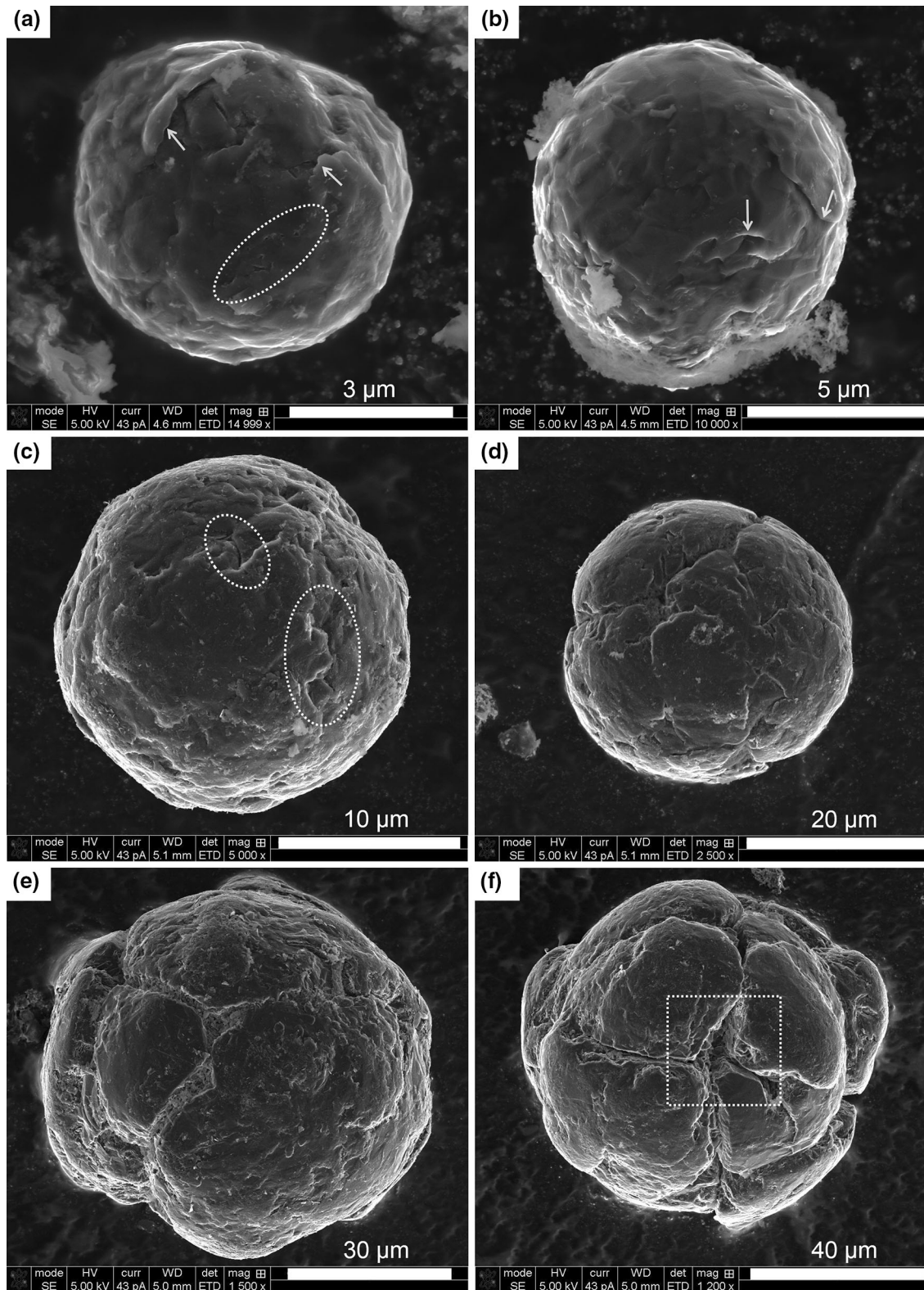
Fig. 17—Secondary electron microscopy images of graphite particles extracted by deep etching. Diameters of the particles are six microns (*a*), nine microns (*b*), 20 μm (*c*), 33 μm (*d*), 74 μm (*e*), and 80 μm (*f*), respectively. (a) and (b) were from the 5-s quenched specimen using the tubular mold, and (c)–(d) were from the directly quenched specimen using a spherical sampler, and (e) and (f) were from the unquenched specimen using a spherical sampler.
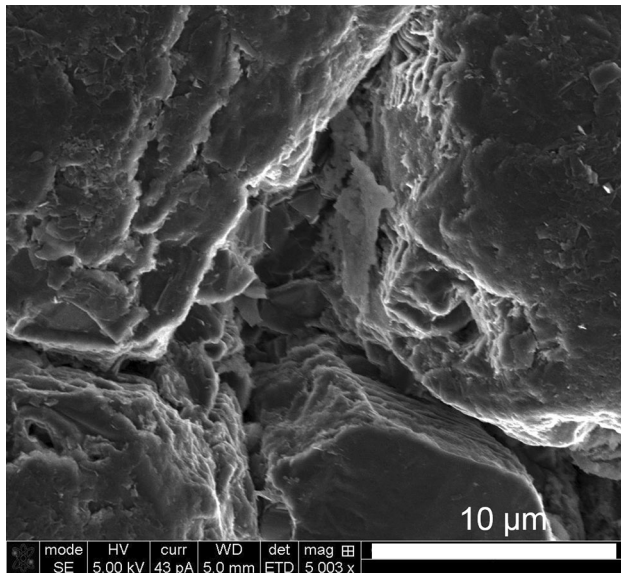
Fig. 18—A magnified image of the region outlined by the dotted box in Fig. 16(f). Faceted growth ledges developed from different sources stopped growing at the gaps which were originally filled with matrix. The matrix was removed during deep etching. Growth ledges made of graphene layers in each conical substructure stacked on each other along the radial directions of the nodule.

Fig. 19—A conical substructure (indicated by the arrow) protruding longer than the other conical substructures in a graphite particle.

There were multiple sources in a graphite nodule and multiple growth ledges proceeded simultaneously to cover the entire surface of a nodule in the early stage. The surface area of a smaller-sized graphite nodule would accommodate a more rapid and complete coverage of each new graphene layer as each propagated circumferentially on the surface, even though not many growth sources were available. Growth fronts from multiple sources would grow until they met. It should be noted that the curvature of a spheroidal graphite particle was large when the diameter of a nodule was small, and many crystallographic defects were required to accommodate the high curvature. Otherwise, holes or small gaps would form due to the mismatch between the growth fronts growing from different sources.

These observed defects and holes may be related to the transition from high coverage sheets to conical substructures. Multiple holes might join together as gaps, and the gaps became deeper and wider during graphite growth. The number count of the sources for the growth steps might increase as the surface area of the graphite nodule increased during growth depending on local undercooling. More gaps would form when more of the growth fronts met but the disregistry was too big to be accommodated by a crystallographic defect. The movement range of the growth front seemed confined by these wide gaps, i.e., the growth front cannot grow past these wide gaps. Gaps due to mismatch became more evident, and a graphite nodule was divided into conical substructures in the later growth stages, even though the curvature became smaller for a larger-sized graphite nodule compared to that for a smaller-sized graphite nodule.

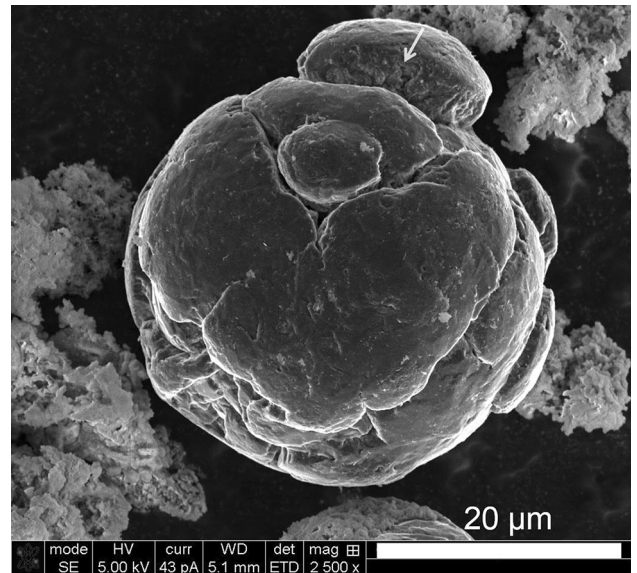Based on the literature, the basal planes of the graphite lattice are normal to the radial directions of a spheroidal graphite particle,[24,25] i.e., the surface of a graphite nodule is mainly made of basal planes. The growth front surfaces which are perpendicular to the radial directions of a nodule are made of prismatic planes. It can be seen that the growth fronts were always propagating circumferentially to the nodule over early growth stages, or at the surface of the conical substructure at later growth stages but stopped at the gaps when the mismatch was too big to be accommodated. More graphene layers were added onto a graphite particle when the growth fronts continued to sweep over the surface of a substructure, and as a result, the size of the particle increased but the net growth direction was along the c- direction (normal of basal plane).

When a graphite nodule was fully in contact with the liquid phase, stress on the graphite nodule from liquid should be small and uniform along different directions and graphene layers would grow more uniformly. However, encroaching austenite produced an anisotropic carbon concentration field around a graphite nodule, and growth of the nodule became uneven. When the solid matrix surrounded a nodule, growth of the graphene layers depended on the carbon diffusion in the matrix, which might vary with different crystallographic directions for the matrix. Moreover, the nodule might be in an anisotropic stress field depending on the crystallographic orientation of the austenite matrix. The traveling distance of a growth step was restricted by carbon diffusion and the growth of a step could not reach the entire surface any more. Meanwhile, the nodule tended to spheroidize in order to minimize the interfacial energy. Therefore, many conical substructures formed in a nodule. Protrusion of conical substructure might be related to partial austenite engulfment, when impurity elements segregated in the liquid phase and lowered down the melting point of remnant liquid. This left a liquid channel next to the graphite, and the graphite–austenite eutectic growth

might be more competitive at this position. In these circumstances, the conical substructures in contact with liquid would grow faster which became longer than the others in a graphite nodule, and an example is given in Figure 19. Protuberance of the conical substructure might initiate the formation of degenerate graphite like a compacted shaped graphite particle. The impurity elements might affect the growth rate of graphite, and this merits additional research.

F. *Future Work*

Ductile iron used in this study is a hypereutectic alloy, thus the solidification process may be different for a hypoeutectic iron alloy or a eutectic iron alloy, which needs further investigation. To better understand the growth of a spheroidal graphite particle, the future work will examine the internal crystallographic structures and defects of the spheroidal graphite particles using the transmission electron microscopy.

This paper studied nodular graphite growth from the standpoint of surface feature evolution in graphite nodules. A transmission electron microscopy (TEM) study of nodular graphite growth based on analysis of the cross sections of graphite nodules is being summarized in another separate paper.

It is well known that there is a correlation between graphite size or size distribution to ductile iron mechanical property. For example, late graphite inoculation (one will see a second or a third graphite size distribution peak) can decrease the shrinkage tendency in ductile iron castings. Post-inoculation of ductile iron may produce different graphite size distributions. The austenite grain size or grain population affects the mechanical properties as well. Regarding multiple growth stages for graphite nodules, uncontrolled later-stage growth may lead to undesired explodes graphite particles or degenerate graphite particles, which may be due to impurity elements. Investigation on the aforementioned effects will be included in the future work.

IV. CONCLUSIONS

The structures of a ductile iron alloy during early solidification stages supported a divorced eutectic solidification model, without coupled growth of graphite and austenite at the solid/liquid front. The spheroidal graphite particles were isolated from liquid phase by an austenite shell after early solidification stages. The following observations support the hypothesis that nucleation of graphite and austenite occurred independently to a significant extent:

(1) statistical analysis of nodule aspect ratio and the analysis of prolate-shaped nodules in the microstructure support an independent nucleation model;
(2) graphite nodules were either trapped in between the austenite dendrite arms or encapsulated by the tip of the austenite dendrite arm;

(3) multiple graphite nodules were engulfed by a single austenite dendrite.

Diameters of graphite particles were small and their growths were limited when the graphite nodules were in contact with the liquid. Graphite particles protruded toward encroaching austenite due to the higher carbon concentrations in front of austenite. Austenite wetted and engulfed graphite nodules once two phases were in contact. The graphite diameter corresponding to austenite shell completion was statistically determined to be six to ten microns.

The growth of graphite nodules proceeded (1) initially by growing curved graphene layers circumferentially around the entire surface with few sources for growth ledges, and (2) later on by growing graphene layers circumferentially within many conical substructures but the growth stopped at the gaps between substructures. The gap formation might result from the large mismatch between growth fronts or the matrix constraint, either diffusion wise or strain wise.

APPENDIX

Growth rate for a graphite nodule in contact with liquid can be estimated using the following equation (from 44):

$$\dot{r}_L = \frac{1}{2r_L} \frac{\left(C^{L/\gamma} - C^{L/Gr}\right)}{\left(C^{Gr} - C^{L/Gr}\right)} \frac{\rho^L}{\rho^{Gr}} D_c^L, \qquad [2]$$

where $C^{L/\gamma}$ is the carbon concentration in liquid at liquid/austenite interface, $C^{L/Gr}$ is the carbon concentration in liquid at liquid/graphite interface, C^{Gr} is the carbon concentration in graphite, ρ^L is the density of liquid (~6.90 g/cm^3), and ρ^{Gr} is the density of graphite (~2.26 g/cm^3), and D_c^L is the carbon diffusivity in liquid [~1 × 10^{-4} cm^2/s at 1423 K (1150 °C)], and r_L is the diameter for graphite nodule in contact with liquid. For a graphite nodule of ~6 μm diameter (in contact with liquid), the calculated growth rate at 1423 K (1150 °C) is 51 μm/s using the data given in Table II.

Growth rate for a graphite nodule surrounded by austenite shell can be calculated using the following equation (from 44):

$$\dot{r}_\gamma = \frac{1.911}{r_\gamma} \frac{\left(C^{\gamma/\mathrm{L}} - C^{\gamma/\mathrm{Gr}}\right)}{\left(1 - C^{\gamma/\mathrm{Gr}}\right)} \frac{\rho^\gamma}{\rho^{\mathrm{Gr}}} D_c^\gamma (1 - f_s)^{2/3}, \quad [3]$$

where f_s is the solid fraction, $C^{\gamma/\mathrm{L}}$ is the carbon concentration in austenite at austenite/liquid interface, and $C^{\gamma/\mathrm{Gr}}$ is the carbon concentration in austenite at austenite/graphite interface, ρ^γ is the density of austenite ($\sim$7.96 g/cm^3), and ρ^{Gr} is the density of graphite ($\sim$2.26 g/cm^3), and D_c^γ is the carbon diffusivity in austenite [$\sim 1 \times 10^{-6}$ cm^2/s at 1423 K (1150 °C)], and r_γ is the diameter of graphite nodule engulfed by austenite. For a graphite nodule of $\sim$10 μm diameter (engulfed by austenite), the calculated growth rate at 1423 K (1150 °C) is 0.34 μm/s.

These calculations estimated the growth rates of graphite nodules from the stand point of carbon diffusion. However, actual graphite growth is much more complicated which may be affected by many other factors like graphite nucleation.

REFERENCES

1. W. Kurz and D.J. Fisher: *Fundamentals of Solidification*, 3edrd ed., Trans Tech Publications, Rockport, 1989.
2. H. Jones and W. Kurz: *Metall. Trans. A*, 1980, vol. 11A, pp. 1265–73.
3. M. Hillert, and V.V. Subba-Rao: *J. Iron Steel Inst.*, 1968, vol. 110, pp. 204–12.
4. H. Fredriksson, and B. Remaeus: *The Metallurgy of Cast Iron: Proceedings of the Second International Symposium on the Metallurgy of Cast Iron*, Georgi Publishing, Geneva, 1974, pp. 315–26.
5. D. M. Stefanescu, and D. K. Brandyopadhyay: *Physical Metallurgy of Cast Iron IV: Proceedings of the Fourth Intl Symposium Held in Tokyo*, Materials Research Society, Tokyo, 1990, pp. 15–26.
6. H. Hecht and J.C. Margerie: *Mem. Sci. Rev. Metall.*, 1971, vol. 68, pp. 325–38.
7. H. Fredriksson, J. Stjerndahl, and J. Tinoco: *Mater. Sci. Eng. A*, 2005, vols. 413–414, pp. 363–72.
8. B. Lux, F. Mollard, and I. Minkoff: *The Metallurgy of Cast Iron: Proceedings of the Second International Symposium on the Metallurgy of Cast Iron*, Georgi Publishing, Geneva, 1974, pp. 371–400.
9. E. Scheil, and L. Hutter: *Archiv fur das Eisenhuttenwesen*, 1953, Mai/Juni, pp. 237–46.
10. *Solidification of Eutectic Alloys: Cast Iron, Casting, ASM Handbook*, ASM International, Metals Park, 2008, vol. 15, pp. 317–29.
11. R. Boeri and F. Weinberg: *AFS Trans.*, 1989, vol. 97, pp. 179–84.
12. G. Rivera R. Boeri, and J. Sikora: *AFS Trans.*, 2003, vol. 111, pp 3–159, pp. 979–89.
13. C.A. Van de Velde: *Keith D. Millis World Symposium on Ductile Iron, Hilton Head, South Carolina*, American Foundry Society, 1998, pp. 143–87.
14. R. Ruxanda, L. Beltran-Sanches, J. Massone, and D.M. Stefanescu: *AFS Trans.*, 2001, vol. 109, p. 37.
15. S.V. Subramanian, D.A.R. Kay, and G.R. Purdy: *MRS Proceedings*, 1984, vol. 34, p. 47.
16. A.N. Roviglione and J.D. Hermida: *Metall. Mater. Trans. B*, 2004, vol. 35, pp. 313–30.
17. I. Minkoff, and B. Lux: *The Metallurgy of Cast Iron: Proceedings of the Second International Symposium on the Metallurgy of Cast Iron*, Georgi Publishing, Geneva, 1974, pp. 473–91.
18. I. Minkoff: *Mater. Res. Soc. Symp. Proc.*, 1985, vol. 34, pp. 37–45.
19. D.D. Double and A. Hellawell: *Acta Metallurgica*, 1974, vol. 22, pp. 481–87.
20. P. Zhu, R. Sha, and Y. Li: *Mater. Res. Soci. Symp. Proc.*, 1984, vol. 34, pp. 3–27.
21. D.D Double and, A. Hellawell: *The Metallurgy of Cast Iron: Proceedings of the Second International Symposium on the Metallurgy of Cast Iron*, Georgi Publishing, Geneva, 1974, pp. 509–28.
22. B. Lux, I. Minkoff, F. Mollard, and E. Thury: *The Metallurgy of Cast Iron: Proceedings of the Second International Symposium on the Metallurgy of Cast Iron*, Georgi Publishing, Geneva, 1974, pp. 495–508.
23. M. Heerschap, P. Delavignette, and S. Amelyncks: *Carbon*, 1964, vol. 1, pp. 235–38.
24. B. Miao, D.O. North Wood, W. Bian, K. Fang, and M.H. Fan: *J. Mater. Sci.*, 1994, vol. 29, pp. 255–61.
25. B. Miao, K. Fang, and W. Bian: *Acta Metal. Mater.*, 1990, vol. 38, pp. 2167–74.
26. A. Shaahin and A. Reza: *Carbon*, 2013, vol. 51, pp. 110–23.
27. A. Shaahin and K. Haamun: *Acta Mater.*, 2012, vol. 60 (20), pp. 7123–31.
28. F.H. Buttner, H.F. Taylor, and J. Wulff: *J. Am. Foundrym.*, 1951, vol. 20, pp. 49–50.
29. E. Selcuk: *The Metallurgy of Cast Iron: Proceedings of the Second International Symposium on the Metallurgy of Cast Iron*, Georgi Publishing, Geneva, 1974, pp. 409–22.
30. S. Jung, T. Ishikawa, and H. Nakae: *Mater. Sci. Eng. A*, 2008, vol. 476, pp. 350–56.
31. R.H. McSwain, and C.E. Bates: *The Metallurgy of Cast Iron: Proceedings of the Second International Symposium on the Metallurgy of Cast Iron*, Georgi Publishing, Geneva, 1974, pp. 423–42.
32. D. Sichen: in *Fundamentals of Metallurgy*, S. Seetharaman, ed., Woodhead Publishing in Materials, Cambridge, 2005.
33. J. Qing, V.L. Richards, and D.C. Van Aken: *AFS Trans.*, 2015, vol. 120, pp. 15-072.
34. M. Xu, S.N. Lekakh, C. Mahimkar, V.L. Richards, and S.A. Dutler: *AFS Trans.*, 2012, vol. 120, pp. 229–36.
35. M.D. Chaudhari, R.W. Heine, and C.R. Loper: *AFS Trans.*, 1974, vol. 82, pp. 431–40.
36. J. Qing, V.L. Richards, and D.C. Van Aken: *Advances in the Science and Engineering of Casting Solidification: An MPMD Symposium Honoring Doru Michael Stefanescu*, Wiley, New York, 2015, pp. 277–85.
37. P.H. Draper and B. Lux: *The Metallurgy of Cast Iron*, Georgi Publishing, Geneva, 1984, pp. 371–400.
38. C.H.P. Lupis: *Chemical Thermodynamics of Materials*, North Holland, Amsterdam, 1983, pp. 365–74.
39. S.N. Lekakh, J. Qing, V.L. Richards, and K.D. Peaslee: *AFS Transactions*, 2013, Paper No. 13–1321.
40. S.E. Wetterfall, H. Fredriksson, and M. Hillert: *J. Iron Steel Inst.*, 1972, vol. 210, p. 23.
41. G. Paul: *J. S. Afr. Inst. Min Metall.*, January 1972, vol. 112, pp. 165–70.
42. B. Goetze, and U. Rosenblatt: *13th Biennial Conference on Carbon*, The American Carbon Society, Irvine, CA, 1977, pp. 334–35.
43. A.W. Adamson: *Physical Chemistry of Surfaces*, 4th ed., Wiley, New York, 1983, pp. 337–38.
44. S.C. Murcia, E.A. Ossa, and D.J. Celentano: *Metall. Mater. Trans. B*, 2014, vol. 45, pp. 707–18.